# San José State University Charles W. Davidson College of Engineering Department of Mechanical Engineering ME 260, Applied Stress Analysis Section 01 (41171), Spring 2023 Dr. Eduardo Chan

Stress Concentration in Airplane Fuselage due to Window Shape

Group 3:

Troy Schmidt (016764293)
David Pokras (011199721)
Niels Hofmeijer (013770510)

#### **Abstract**

In this project a stress analysis is performed on the fuselage of an airplane. Analytical and finite element models are used to solve for stress distributions and stress concentration factors around circular and square windows. Then, the solutions from these models are compared. The outcome of the project shows that the analytical model involves assumptions that underestimate the stresses. Finite element analysis is more realistic as it contains less assumptions than the analytical method. For a circular hole the stresses in FEA were 11% higher than in the analytical model. Furthermore, it was found that a square hole with a corner radius over width ratio of 0.2 results in 1.75 times higher stresses than for a circular hole. Finite element modeling is recommended for problems like this as it provides more realistic results. These results can be validated by experiments such as strain gauges and digital image correlation.

#### Introduction

Windows are an essential component of aircrafts, and pose a challenging engineering problem. As important as it is for the experience of an aircraft passenger to have windows, engineers must design these windows to withstand the intrinsic stress concentrations they impose on the aircraft. As history has proven, accurately calculating and designing for the concentrations around passenger windows is not easy.

The first commercial jet airliner, the Havilland DH 106 Comet, used square windows that were later modified to circular windows. According to the Federal Aviation Administration, the square windows of the Havilland airplane created "stress concentrations much higher than anticipated. These stress concentrations fatigued the material around the window corners, which would quickly lead to a rupture of the fuselage" ("De Havilland DH106 Comet 1 & 2").



Figure 1: Havilland DH 106 Comet airplane, the world's first commercial airliner, square windows ("De Havilland DH106 Comet 1 & 2")



Figure 2: Havilland DH 106 Comet airplane after windows were modified to be circular (Beresnevicius and Mickeviciute)

In modern commercial airplanes, passenger windows have now been modified to be rectangular with filleted corners. This both relieves stress concentrations around the windows, and also maximizes passenger experience by having a large viewing area.



Figure 3: Modern airplane passenger windows ("FAA Doesn't Specify How Hot Is Too Hot in a Grounded Airplane")

#### **Objective**

In this report, stress concentrations around window cutouts in an airplane's fuselage will be analyzed. By analyzing different shapes of windows, such as circular and square with fillets, the effect of window shape on stress concentrations will be determined. With these results, the reinforcement requirements in the airplane's fuselage substructure could be determined.

A comparative analysis of the airplane's skin will be performed between analytical calculations and finite element analysis (FEA). The results of these two solution methods will then be compared to determine the accuracy, identify potential discrepancies, and assess the reliability of both methods. Experimental validation methods will then be explored as possible ways that this analysis could further be tested in industry.

# Methodology

Aerospace engineering and the complexity of aircraft design requires years of research involving large teams. For the purpose of this report, several assumptions need to be made to reduce the engineering problem to a manageable complexity. Throughout the analytical solution the assumptions

Table 1: Initial Modeling Assumptions

Modeling Assumptions					
Assumption	Explanation				
Material: stainless steel	Stainless steel is commonly used in aircrafts for its durability and longevity.  E = 190 GPa (@ -60° C)  v = 0.265  Linear elastic, isotropic				
Airplane fuselage is perfectly tubular	This will simplify the stress analysis around the passenger windows.				
Plane outer diameter: 6324 mm	This is the approximate diameter of a typical airplane fuselage.				
Airplane skin thickness: 2 mm	This is the approximate thickness of a typical airplane skin.				
The stainless steel airplane skin is the material that endures the radial loading due to gauge pressure.	There may be a lining that seals the airplane cabin adjacent to the stainless steel sheathing, but the lining would not resist stresses due to pressurization, the stainless steel sheathing does.				
Airplane is flying at 11,000 m	Interior cabin pressure: 76,000 Pa Exterior pressure: 22,600 Pa Gauge pressure = 53,400 Pa Air temperature: -60° C				
Exterior of plane is frictionless	The stress distribution due to airspeed and turbulence is neglected.				
Static loading conditions	The airplane is assumed in steady-flight, with no variations in loading.				
The passenger windows are 305 mm x 305 mm, with fillet sizes ranging from 15.25 mm to 152.5 mm (circle window).	To simplify the analytical model, this is the assumed window size to analyze.				
Stress distributions do not change due to fatigue	This project aims to directly compare analytical and FEA solutions, and fatigue is beyond the scope of the project and the class				



Figure 4: Cross-section of an airplane fuselage (Syracuse Hancock International Airport)

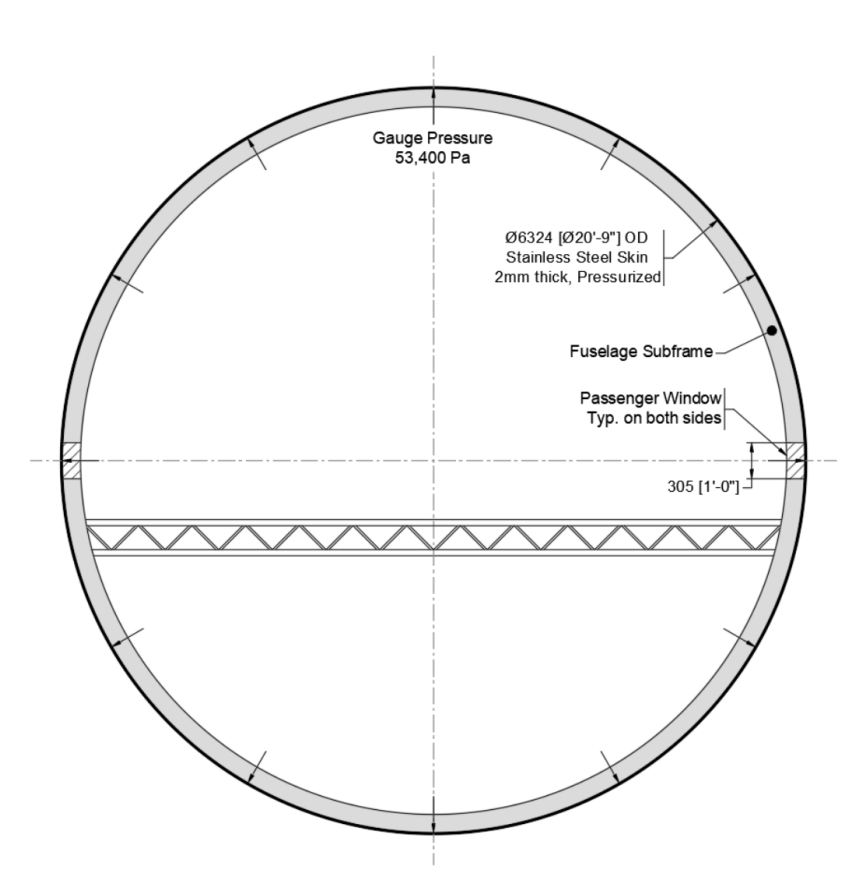


Figure 5: Diagram of assumed airplane fuselage cross-section

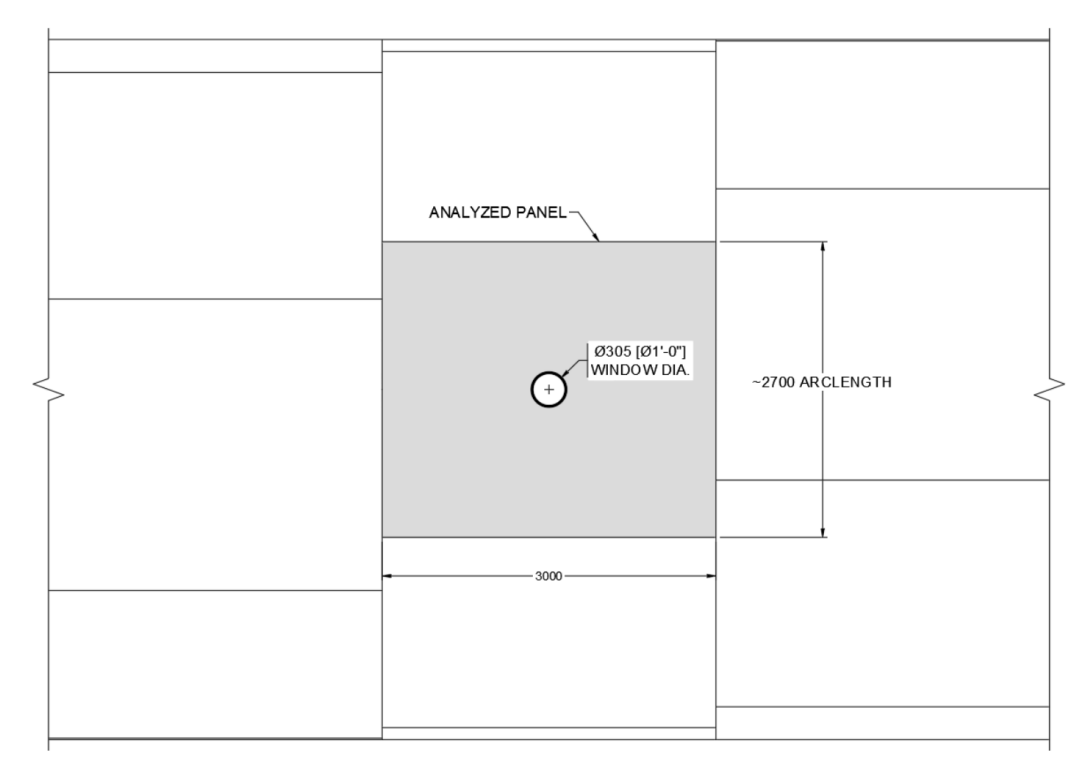


Figure 6: Stainless steel panel of airplane skin side view

The radius of the plane is more than 10 times larger than the thickness of the plane. Hence, a thin-wall cylinder can be assumed. The thin-wall cylinder approach provides stresses for the longitudinal direction and the tangential direction of the cylinder. Now, a small section (plate) of the fuselage around the window can be considered. Due to the large radius of the cylinder and to simplify the problem this plate is assumed to be flat while in reality this plate will be curved. The longitudinal and tangential stresses of the cylinder cause a biaxial loading on the plate with the window (hole) as shown in Figure 1. For circular windows, Airy stress functions and superposition will be used to determine the final stress distribution and concentration factor for circular windows. For rectangular windows, Roark's formulas for stress and strain will be used to determine the stress concentration factor.

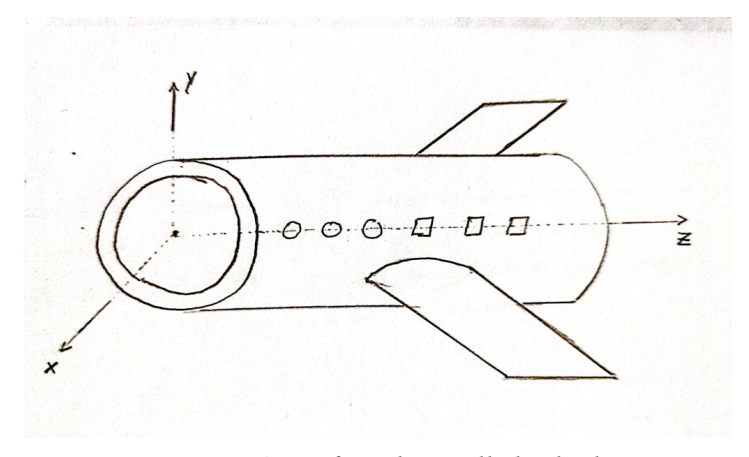


Figure 7: Aircraft as thin-walled cylinder

The analytical solutions will be compared to the finite element model. Using ANSYS FEA software, the entire fuselage will be modeled and the internal and external pressures will be applied. Double symmetry will be used to decrease the size of the model. On the symmetry lines, the model will be constrained with frictionless supports. Both the circular and the rectangular windows will be analyzed for stress using FEA. Lastly, for the rectangular window, a parameter study will be executed to illustrate the impact of the window's corner radius on the stress concentration.

#### **Analytical Calculations**

#### **Pressurized Thin-Walled Cylinder Approach**

As discussed in the methodology, for the aircraft, a thin-wall cylinder can be assumed. The inside pressure of the aircraft is higher than the outside pressure. This pressure induces stresses in the longitudinal direction (z-direction) and the tangential direction (*Figure 2*). The tangential stress or "hoop" stress can be determined using equilibrium equations:

$$\Sigma F_{x} = F_{p} + F_{h} = 0$$

where  $F_p$  is the force induced by the pressure and  $F_h$  is the force induced by the hoop stress. Multiplying stress with area gives these forces:

$$p(r_p \Delta \theta) \Delta z - 2\sigma_h sin\left(\frac{\Delta \theta}{2}\right) t \Delta z = 0$$

where t represents the thickness of the fuselage and  $r_p$  is the radius of the cylinder (plane). So now the hoop stress can be expressed as:

$$\sigma_h = \frac{pr_p}{t}$$

Using a similar approach, the longitudinal stress can be found. Knowing that the aircraft is enclosed, the equilibrium equation becomes:

$$\Sigma F_z = F_p + F_z = 0$$

where  $F_z$  is the force induced by the longitudinal stress. Multiplying stress with area gives these forces:

$$p(\pi r_p^2) - \sigma_z(2\pi r_p)t = 0$$

Therefore longitudinal stress can be expressed as:

$$\sigma_{z} = \frac{pr_{p}}{2t}$$

Note that the hoop stress is twice as large as the longitudinal stress ( $\sigma_h = 2\sigma_z$ ).

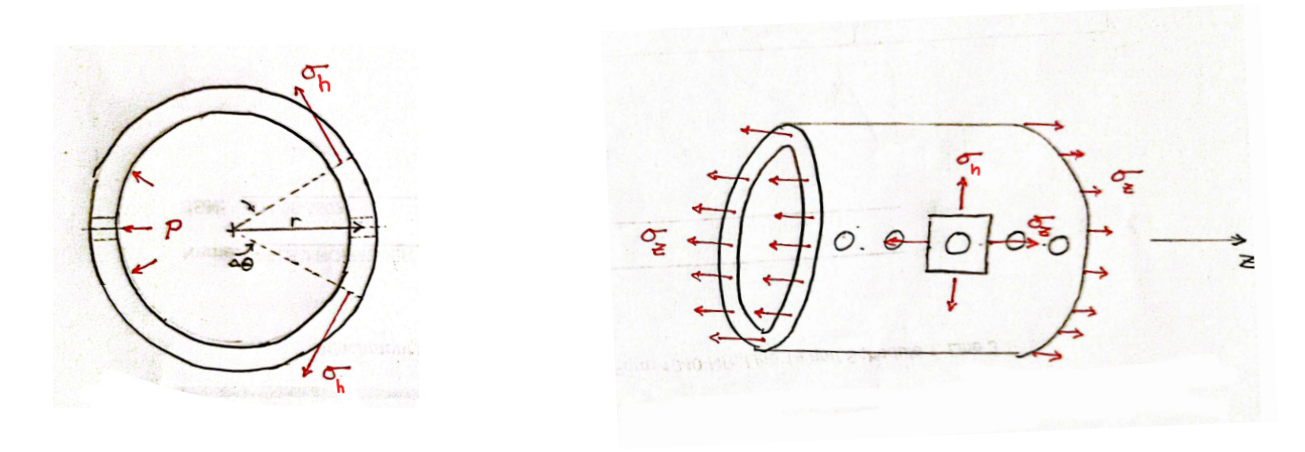


Figure 8: Stresses on a pressurized cylinder

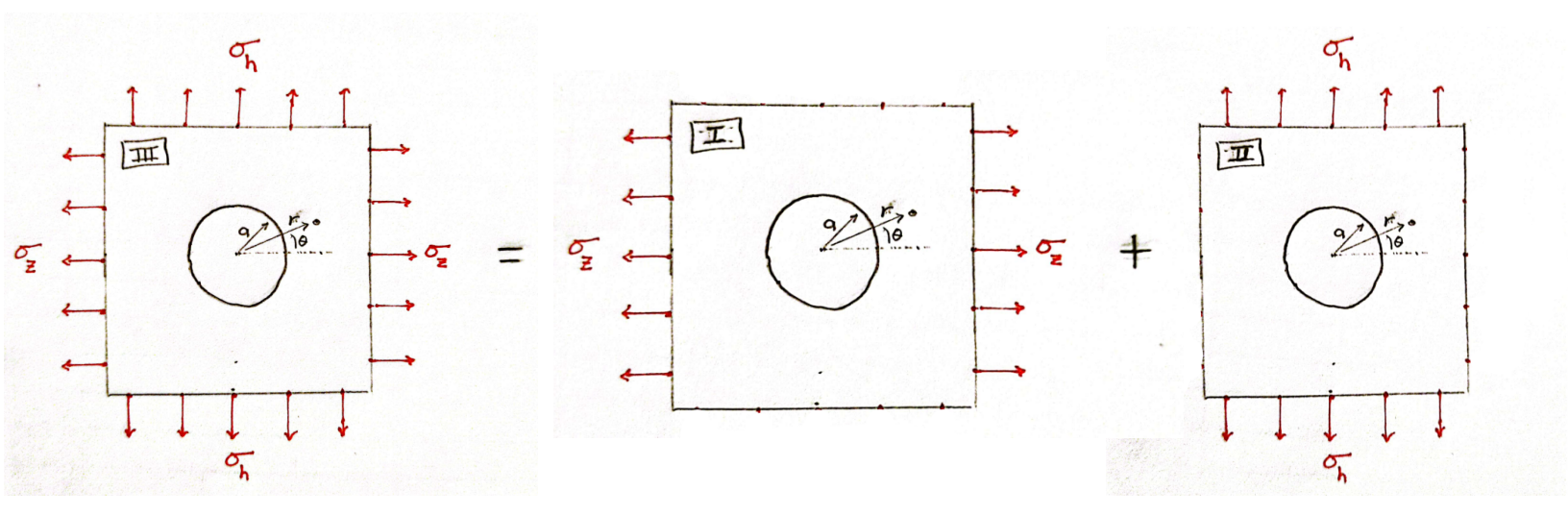


Figure 9: Window under biaxial loading

# **Circular Window Calculations**

To analyze the stresses around the window, the window is assumed to be located on a flat infinite domain subjected to biaxial loading. Airy stress function and superposition will be used to solve for the stress fields (Figure 3). For a plate with a hole under uniaxial tension, the Airy stress function in polar coordinates is expressed by:

$$\Phi = \Phi_1 + \Phi_2(r)cos(2\theta)$$

The Airy stress function should satisfy the biharmonic equation, therefore:

$$\nabla^{4} \Phi = \left( \frac{\partial^{2}}{\partial r^{2}} + \frac{1}{r} \frac{\partial}{\partial r} + \frac{1}{r} \frac{\partial^{2}}{\partial \theta^{2}} \right)^{2} \Phi = 0$$

$$\left( \frac{d^{2}}{dr^{2}} + \frac{1}{r} \frac{d}{dr} \right)^{2} \Phi_{1}(r) + \left( \frac{d^{2}}{dr^{2}} + \frac{1}{r} \frac{d}{dr} - \frac{4}{r} \right)^{2} \Phi_{2}(r) \cos(2\theta) = 0$$

So now  $\phi_1$  and  $\phi_2$  are expressed as:

$$\Phi_1(r) = A + Blog(r) + Dr^2 log(r)$$

$$\Phi_2(r) = E + Fr^2 + Gr^4 + \frac{H}{r^2}$$

Using the Airy stress functions, the radial, tangential, and the shear stress fields can be obtained by using the following equations:

$$\sigma_r = \frac{1}{r^2} \frac{\partial^2 \Phi}{\partial \theta^2} + \frac{1}{r} \frac{\partial \Phi}{\partial r}$$

$$\sigma_{\theta} = \frac{\partial^2 \Phi}{\partial r^2}$$

$$\tau_{r\theta} = \frac{1}{r^2} \frac{\partial \Phi}{\partial \theta} - \frac{1}{r} \frac{\partial^2 \Phi}{\partial r \partial \theta}$$

Plugging Equation # into Equation # results in the expressions:

$$\sigma_{r} = \frac{B}{r^{2}} + 2C + D(1 + 2log(r)) - \left(\frac{4E}{r^{2}} + \frac{6F}{r^{4}} + 2G\right)cos(2\theta)$$

$$\sigma_{\theta} = -\frac{B}{r^{2}} + 2C + D(3 + 2log(r)) + \left(\frac{6F}{r^{4}} + 2G + 12H\right)cos(2\theta)$$

$$\tau_{r\theta} = \left(-\frac{2E}{r^{2}} - \frac{6F}{r^{4}} + 2G + 6Hr^{2}\right)sin(2\theta)$$

The following boundary conditions will be applied to determine the coefficients of the Airy stress functions:

 $\succ$  Traction free condition at hole (r = a):

$$\circ \quad \sigma_r(a, \, \theta) = \tau_{r\theta}(a, \theta) = 0$$

ightharpoonup The stresses far away from hole  $(r = \infty)$ 

$$\circ \quad \sigma_r(\infty, \theta) = \frac{T}{2} \left( 1 + \cos(2\theta) \right)$$

$$\circ \quad \sigma_{\theta}(\infty, \theta) = \frac{T}{2}(1 - \cos(2\theta))$$

$$\circ \quad \tau_{r\theta}(\infty,\theta) = -\frac{T}{2}sin(2\theta)$$

where T is the uniaxial tension. Using Equation #, #, #, the coefficients are found to be:

$$>$$
  $A = D = H = 0$ 

$$> B = - E = - 2F = \frac{-Ta^2}{2}$$

$$\triangleright$$
  $C = -G = \frac{T}{4}$ 

Hence, the stress fields for situation I (Figure 3) becomes:

$$\sigma_{r_{I}} = \frac{\sigma_{z}}{2} \left( 1 - \frac{a^{2}}{r^{2}} \right) + \frac{\sigma_{z}}{2} \left( 1 + \frac{3a^{4}}{r^{4}} - \frac{4a^{2}}{r^{2}} \right) cos(2\theta)$$

$$\sigma_{\theta_{I}} = \frac{\sigma_{z}}{2} \left( 1 + \frac{a^{2}}{r^{2}} \right) - \frac{\sigma_{z}}{2} \left( 1 + \frac{3a^{4}}{r^{4}} \right) cos(2\theta)$$

$$\tau_{r\theta_{I}} = -\frac{\sigma_{z}}{2} \left( 1 - \frac{3a^{4}}{r^{4}} + \frac{2a^{2}}{r^{2}} \right) sin(2\theta)$$

The stress fields from situation II (Figure 3) can be determined by rotating the situation I by 90 degrees. Substituting  $\sigma_z$  for  $\sigma_h$  and  $\theta_{II} = \theta + \frac{\pi}{2}$  in the stress field equations of situation I will provide the stress fields for situation 2:

$$\begin{split} &\sigma_{r_{II}} = \frac{\sigma_{h}}{2} \left( 1 - \frac{a^{2}}{r^{2}} \right) + \frac{\sigma_{h}}{2} \left( 1 + \frac{3a^{4}}{r^{4}} - \frac{4a^{2}}{r^{2}} \right) cos(2\theta + \pi) = \frac{\sigma_{h}}{2} \left( 1 - \frac{a^{2}}{r^{2}} \right) - \frac{\sigma_{h}}{2} \left( 1 + \frac{3a^{4}}{r^{4}} - \frac{4a^{2}}{r^{2}} \right) cos(2\theta) \\ &\sigma_{\theta_{II}} = \frac{\sigma_{h}}{2} \left( 1 + \frac{a^{2}}{r^{2}} \right) - \frac{\sigma_{h}}{2} \left( 1 + \frac{3a^{4}}{r^{4}} \right) cos(2\theta + \pi) = \frac{\sigma_{h}}{2} \left( 1 + \frac{a^{2}}{r^{2}} \right) + \frac{\sigma_{h}}{2} \left( 1 + \frac{3a^{4}}{r^{4}} \right) cos(2\theta) \\ &\tau_{r\theta_{II}} = -\frac{\sigma_{h}}{2} \left( 1 - \frac{3a^{4}}{r^{4}} + \frac{2a^{2}}{r^{2}} \right) sin(2\theta + \pi) = \frac{\sigma_{h}}{2} \left( 1 - \frac{3a^{4}}{r^{4}} + \frac{2a^{2}}{r^{2}} \right) sin(2\theta) \end{split}$$

Using superposition, the stress fields for the biaxial stress (III, Figure 3) are:

$$\begin{split} &\sigma_{r} = \sigma_{r_{I}} + \sigma_{r_{II}} \\ &= \frac{\sigma_{z}}{2} \bigg[ \bigg( 1 - \frac{a^{2}}{r^{2}} \bigg) + \bigg( 1 + \frac{3a^{4}}{r^{4}} - \frac{4a^{2}}{r^{2}} \bigg) cos(2\theta) \bigg] + \frac{\sigma_{h}}{2} \bigg[ \bigg( 1 - \frac{a^{2}}{r^{2}} \bigg) - \bigg( 1 + \frac{3a^{4}}{r^{4}} - \frac{4a^{2}}{r^{2}} \bigg) cos(2\theta) \bigg] \\ &\sigma_{r} = \frac{\sigma_{z} + \sigma_{h}}{2} \bigg( 1 - \frac{a^{2}}{r^{2}} \bigg) + \frac{\sigma_{z} - \sigma_{h}}{2} \bigg( 1 + \frac{3a^{4}}{r^{4}} - \frac{4a^{2}}{r^{2}} \bigg) cos(2\theta) \\ &\sigma_{\theta} = \sigma_{\theta_{I}} + \sigma_{\theta_{II}} \\ &= \frac{\sigma_{z}}{2} \bigg[ \bigg( 1 + \frac{a^{2}}{r^{2}} \bigg) - \bigg( 1 + \frac{3a^{4}}{r^{4}} \bigg) \bigg] cos(2\theta) + \frac{\sigma_{h}}{2} \bigg[ \bigg( 1 + \frac{a^{2}}{r^{2}} \bigg) + \bigg( 1 + \frac{3a^{4}}{r^{4}} \bigg) \bigg] cos(2\theta) \\ &\sigma_{\theta} = \frac{\sigma_{z} + \sigma_{h}}{2} \bigg( 1 - \frac{a^{2}}{r^{2}} \bigg) + \frac{\sigma_{h} - \sigma_{z}}{2} \bigg( 1 + \frac{3a^{4}}{r^{4}} \bigg) cos(2\theta) \end{split}$$

$$\begin{split} \tau_{r\theta} &= \tau_{r\theta_{I}} + \tau_{r\theta_{II}} \\ &= -\frac{\sigma_{z}}{2} \left( 1 - \frac{3a^{4}}{r^{4}} + \frac{2a^{2}}{r^{2}} \right) sin(2\theta) + \frac{\sigma_{h}}{2} \left( 1 - \frac{3a^{4}}{r^{4}} + \frac{2a^{2}}{r^{2}} \right) sin(2\theta) \\ \tau_{r\theta} &= \frac{\sigma_{h}^{-}\sigma_{z}}{2} \left( 1 - \frac{3a^{4}}{r^{4}} - + \frac{2a^{2}}{r^{2}} \right) sin(2\theta) \end{split}$$

From the thin-wall cylinder approach, it is known that:

$$\sigma_h = 2\sigma_z = \frac{pr_p}{t}$$

Therefore,

$$\frac{\sigma_z + \sigma_h}{2} = \frac{3pr_p}{4t}$$

$$\frac{\sigma_z - \sigma_h}{2} = \frac{-pr_p}{4t}$$

$$\frac{\sigma_h - \sigma_z}{2} = \frac{pr_p}{4t}$$

Now, the stress field equations can be simplified using the terms above:

$$\begin{split} &\sigma_{r}(r,\theta) = \frac{3pr_{p}}{4t} \left( 1 - \frac{a^{2}}{r^{2}} \right) + \frac{-pr}{4t} \left( 1 + \frac{3a^{4}}{r^{4}} - \frac{4a^{2}}{r^{2}} \right) cos(2\theta) \\ &\sigma_{\theta}(r,\theta) = \frac{3pr_{p}}{4t} \left( 1 - \frac{a^{2}}{r^{2}} \right) + \frac{pr}{4t} \left( 1 + \frac{3a^{4}}{r^{4}} \right) cos(2\theta) \\ &\tau_{r\theta}(r,\theta) = \frac{pr_{p}}{4t} \left( 1 - \frac{3a^{4}}{r^{4}} - + \frac{2a^{2}}{r^{2}} \right) sin(2\theta) \end{split}$$

The Von-Mises stress can be expressed as:

$$\sigma_{vm} = \sqrt{\sigma_r^2 - \sigma_r \sigma_\theta + \sigma_\theta^2 + 3\tau_{r\theta}^2}$$

To find the stress concentration, the maximum tangential stress at the hole will be compared to the tangential stress far away from the hole (nominal stress):

$$\sigma_{\theta}(a,\theta) = \frac{3pr}{2t} + \frac{pr}{t}cos(2\theta) \Rightarrow \sigma_{\theta,max} = \frac{5pr}{2t}$$
$$\sigma_{\theta}(\infty,\theta) = \frac{3pr}{4t} + \frac{pr}{4t}cos(2\theta) \Rightarrow \sigma_{\theta,nom} = \frac{pr}{t}$$

The stress concentration in this model at the hole will be:

$$K_t = \frac{\sigma_{\theta,max}}{\sigma_{\theta,nom}} = 2.5$$

The stress distributions are plotted by developing a MATLAB code (Appendix A). The radial, tangential, shear, and Von-Mises stresses are shown respectively in Figure 4, 5, 6, and 7.

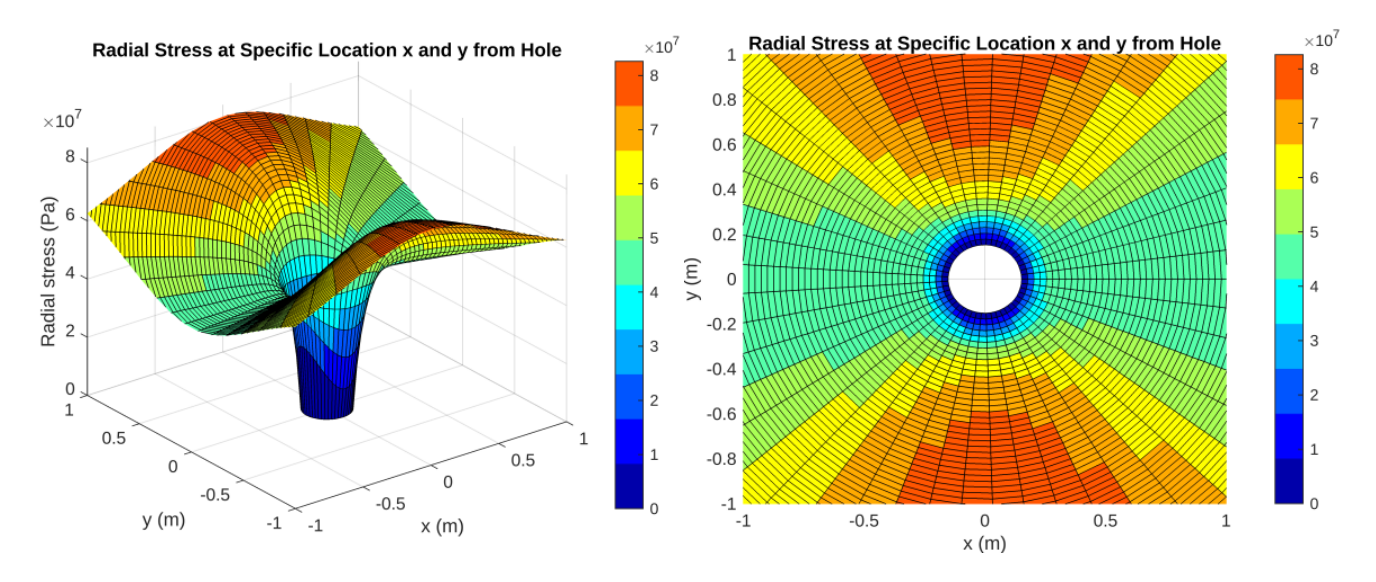


Figure 10: Radial stress distribution 3D plot (left) and top view (right)

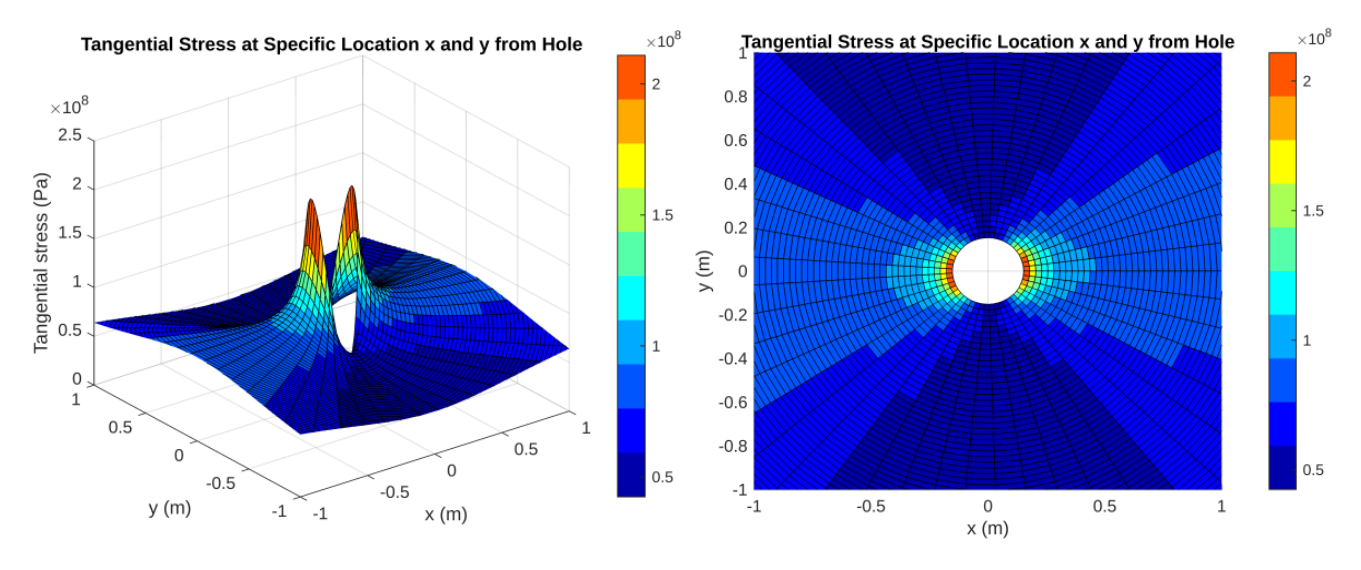


Figure 11: Tangential stress distribution 3D plot (left) and top view (right)

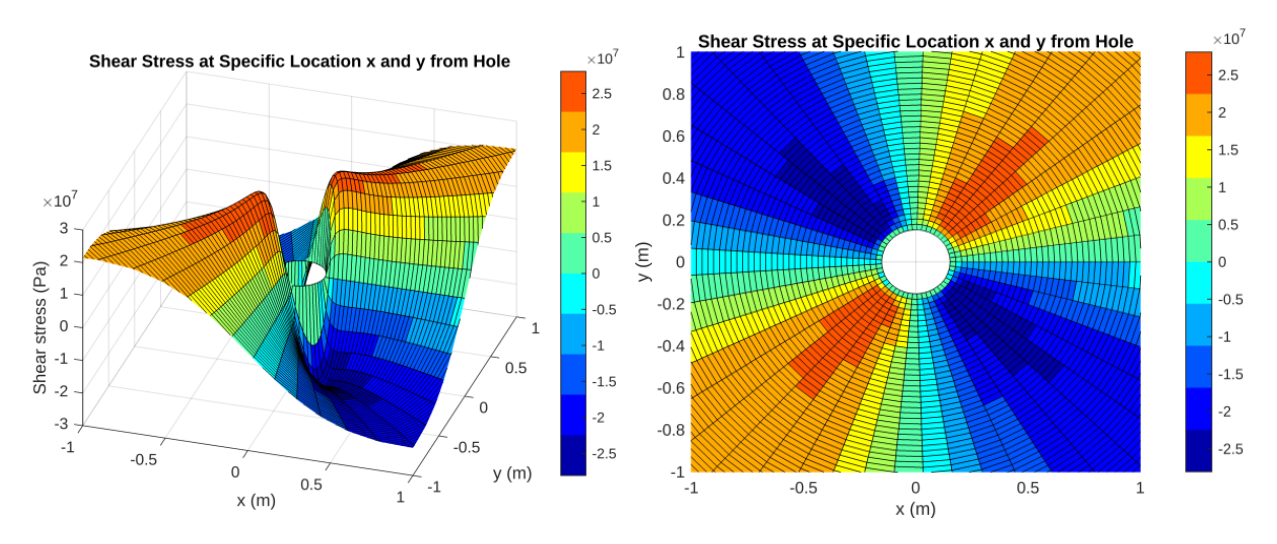


Figure 12: Shear stress distribution 3D plot (left) and top view (right)

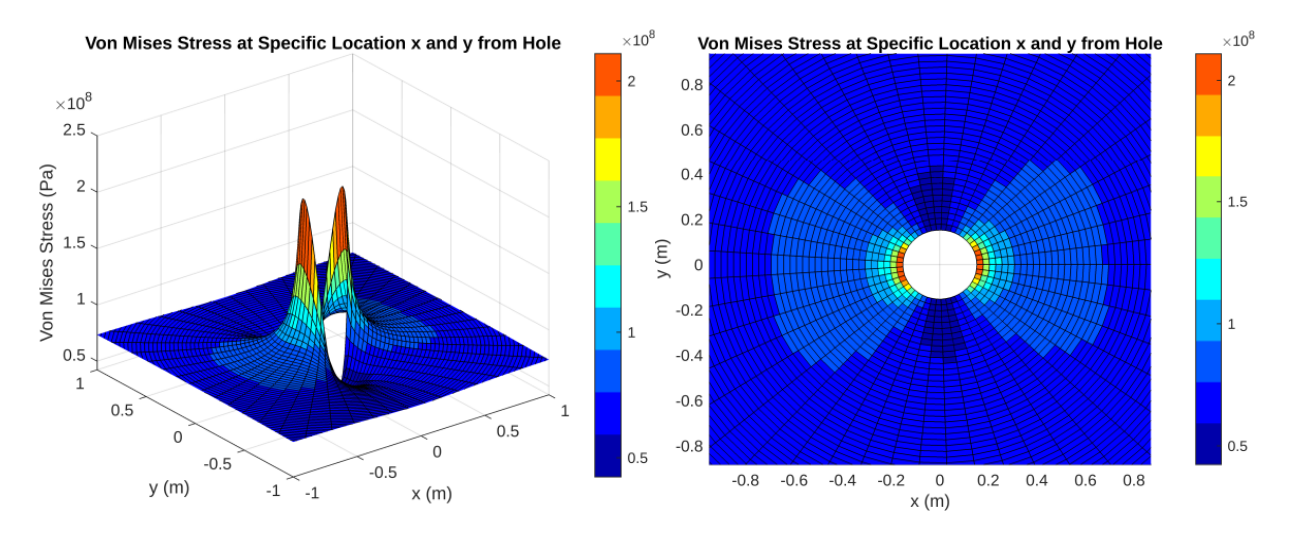


Figure 13: Von-Mises stress distribution 3D plot (left) and top view (right)

The maximum stress quantities are:

Maximum radial stress:
 Maximum tangential stress:
 Maximum shear stress:
 Maximum Von Mises stress;
 211 MPa
 Maximum Von Mises stress;

#### **Square Window Calculations**

For the square windows, this project will focus on the maximum stress. According to the book "Roark's Formulas for Stress and Strain" (Roark and Young 728), the stress concentration factor for a rectangular hole in a plate subjected to uniaxial stress is:

$$K_{t} = K_{1} + K_{2} \left(\frac{b}{a}\right) + K_{3} \left(\frac{b}{a}\right)^{2} + K_{4} \left(\frac{b}{a}\right)^{3}$$

where a and b are the height and width of the hole (Figure 8). For a square window the ratio  $\frac{b}{a}$  equals to 1. Therefore, the stress concentration factor for a square hole will be

$$K_{t} = K_{1} + K_{2} + K_{3} + K_{2}$$

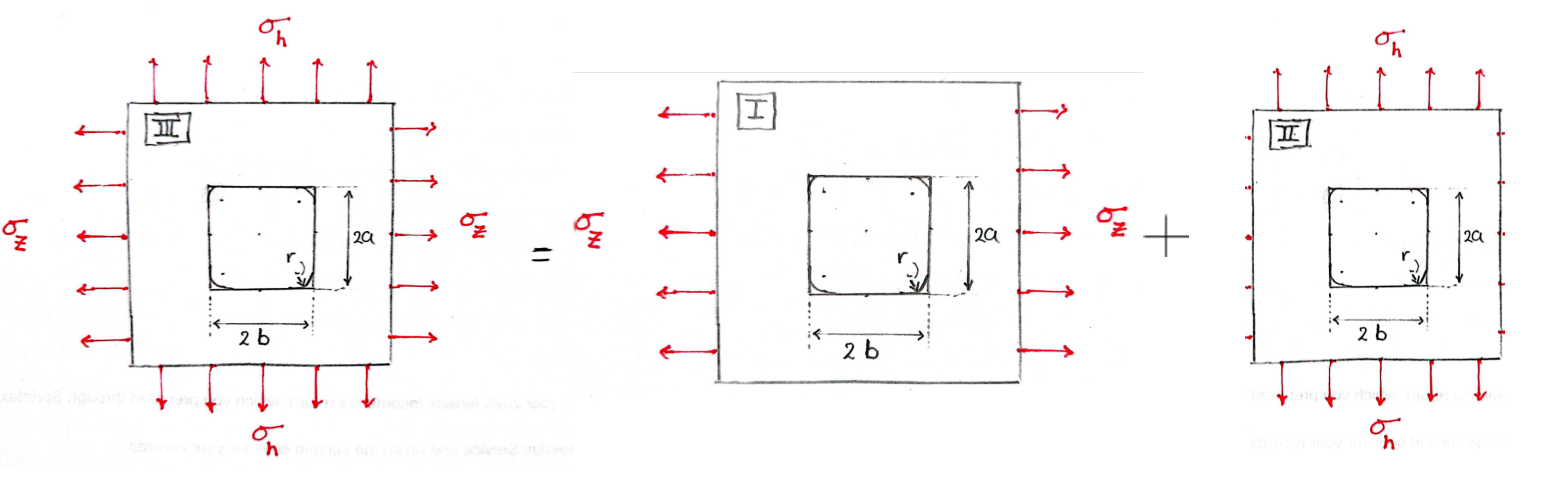


Figure 14: Square window in plate and the superposition

Furthermore, the stress concentration coefficients  $(K_i)$  depend on the ratio of the corner radius (r) over the width of the hole (b). From Roark's book the stress concentration coefficients are:

$$K_1 = 14.815 - 15.774\sqrt{\frac{r}{b}} + 8.149\frac{r}{b}$$

$$K_2 = -11.201 - 9.750\sqrt{\frac{r}{b}} + 9.600\frac{r}{b}$$

$$K_3 = 0.202 + 38.622\sqrt{\frac{r}{b}} - 27.374\frac{r}{b}$$

$$K_4 = 3.232 - 23.002\sqrt{\frac{r}{b}} + 15.482\frac{r}{b}$$

The width of the window (2b) is chosen to be equal to the diameter of the circular window (30.5 cm). The minimum and maximum corner radius in order for Roark's formulas to be valid is 3.05 cm and 15.25 cm respectively. The maximum corner radius would in fact be a circular hole. Using the smaller corner radius (3.05 cm) results in the following stress concentration coefficients for our geometry:

$$K_1 = 9.3905$$
  
 $K_2 = -13.6413$ 

$$> K_3 = 11.9995$$

$$> K_4 = -3.9584$$

Adding the stress concentration coefficients provides the stress concentration factor for a square hole:

$$K_{t} = 3.7902$$

Note that the stress concentration factor is independent of the uniaxial loading. A sensitivity study can be performed by varying the corner radius and recording the stress concentration. For now, only the hoop stress (84.312 MPa) is considered so the maximum stress can be calculated. The results are shown in Table 1 and in Figure 9.

Table 2: Roark's formula for stress concentration

r/b	r (mm)	K1	K2	К3	K4	K_t	Max Stress (MPa)
0.2	30.5	9.390	-13.641	11.999	-3.958	3.790	319.559
0.3	45.75	8.620	-13.661	13.144	-4.722	3.380	285.013
0.4	61	8.098	-13.527	13.679	-5.123	3.127	263.640
0.5	76.25	7.736	-13.295	13.825	-5.292	2.973	250.686
0.6	91.5	7.486	-12.993	13.694	-5.296	2.891	243.712
0.7	106.75	7.322	-12.638	13.354	-5.175	2.862	241.269
8.0	122	7.226	-12.242	12.847	-4.956	2.875	242.413
0.9	137.25	7.185	-11.811	12.205	-4.656	2.924	246.490
1	152.5	7.190	-11.351	11.450	-4.288	3.001	253.020

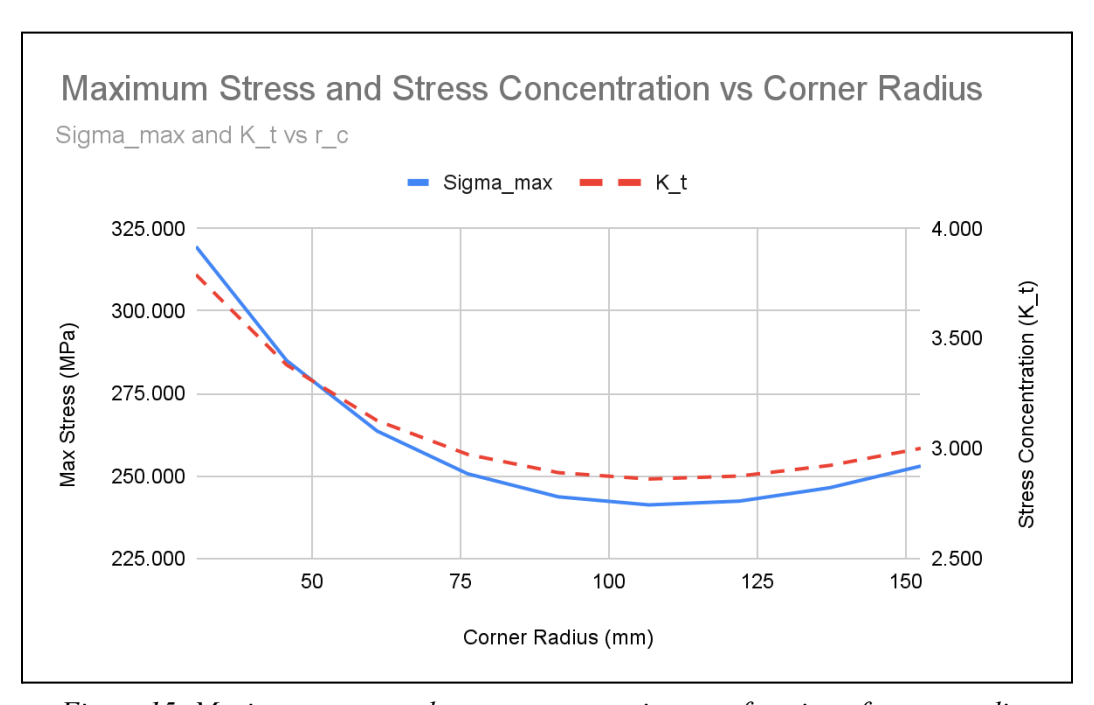


Figure 15: Maximum stress and stress concentration as a function of corner radius

For our case (biaxial stress), the stress concentration factor can be determined using superposition. To use superposition, the stress distribution around the square hole needs to be obtained. Stress distributions of a square hole can be determined by using mapping functions. A rectangular hole in the regular z-plane is mapped into a circular hole in the  $\zeta$ -zeta plane. In the  $\zeta$ -plane, the stress distribution can be obtained for a circular hole similar to our analytical solution of the circular window. The stress distribution of a rectangular plate can be obtained by mapping function the stress distribution of the circular hole in the  $\zeta$ -plane to the z-plane. This operation is executed by the so-called mapping function. The paper "Stress around square and rectangular cutouts in symmetric laminates" studies the stress distribution around a square hole subjected to equi-biaxial stress (*Figure 16*) (Nageswara Rao et al.). Due to the symmetry of the square hole the stress concentration occurs at the internal corners (  $\theta = 45^{\circ}, 135^{\circ}, 225^{\circ}, 315^{\circ}$ ). These high stress locations are the same for a square hole subjected to uniaxial stress according to the paper "Stress analysis of a finite plate with a rectangular hole subjected to

uniaxial tension using modified stress functions" (Pan et al.).

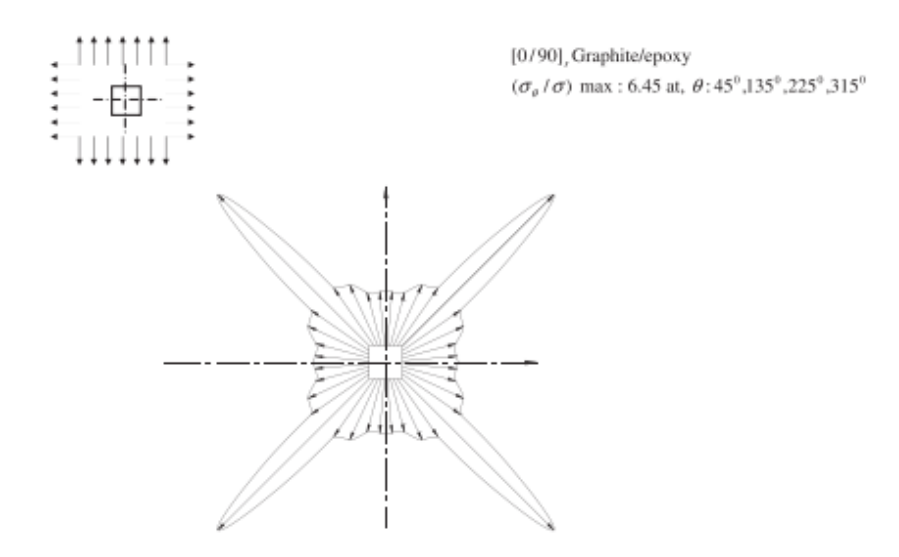


Figure 16: Stress distribution around a square hole under equi-biaxial stress (Nageswara Rao et al.)

The situation that is considered in this project is a biaxial loading where the stress in the horizontal direction (longitudinal stress) is half the stress in the vertical direction (hoop stress). To find the stress concentration factor, this problem can be simplified by thinking of a uniaxial stress as a biaxial stress with one stress (in one axis) being significantly smaller than the stress in the other axis. Roark's formulas (Roark and Young 728) shows that the stress concentration for the uniaxial loading case is 3, whereas an equi-biaxial loading case results in a stress concentration factor of 2. As the smaller stress gets gradually larger, the stress will gradually change from uniaxial to equi-biaxial. Therefore, it is expected that the stress concentration of a circular hole under the condition where stress in one axis is exactly half of the stress in the other axis has to be approximately halfway between 2 and 3. The analytical solution for the circular hole confirms this as the stress concentration was found to be 2.5.

A similar approach will be applied to the square window. *Figure 10* shows that the stress concentration for the biaxial case is 6.45 with a ratio of 0.00692 between the width of the square and the corner radius. For a very similar ratio, the stress concentration of the uniaxial stress was found to be 4.48 (Pan et al.). Hence, the stress concentration for this project will be approximately in the middle of these values, approximately 5.47.

#### **Finite Element Method**

Following the analytical solution, a 3D model was created in ANSYS, a software package capable of finite element analysis. The goal of this is to compare the analytical results to that of a computer simulation. One important consideration in the analytical approach was the methodology used to approximate the solution. First a thin-walled cylinder was assumed to obtain the approximated biaxial stresses in a flat plate with a window cutout. In reality the plate is curved due to the tubular shape of the fuselage. As such, it is expected to see some difference during comparison of the results. The skin of the airplane in a monocoque construction is actually the main structural component (Williams), providing credit to the earlier assumption that the airplane skin, or 2mm outermost layer, is the component of the fuselage which endures the stresses induced by the difference of pressure acting on its inner and outer surfaces. *Figure 17* demonstrates this by showing the internal construction of a monocoque fuselage. For the purpose of this numerical analysis, the sections of the fuselage modeled in ANSYS are also assumed to be located between the Former elements of the fuselage.

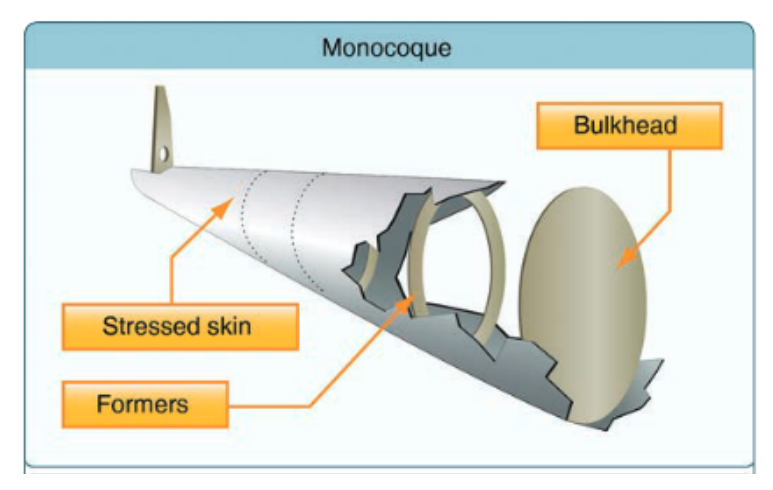


Figure 17: Airplane skin as a main structural component in monocoque fuselages

In an ideal scenario, the 3-dimensional ANSYS model would include the entire fuselage, every structural component down to the rivet, and an incredibly fine mesh to obtain the most detailed and accurate results possible, but that is simply not feasible without a supercomputer. Using the previously stated assumptions, a simplified model of the fuselage is presented in *Figure 18*. This model assumes the fuselage to be an open-ended thin-walled cylinder, validated by satisfying the condition of t < r/10 where the thickness t is equal to 2 mm, and the radius r is equal to 3162 mm. Due to its open-ended nature, longitudinal stress  $\sigma_z$  is assumed to be zero, leaving the skin to only be stressed uniaxially in the tangential direction as a result of the gauge pressure. The initial model of the fuselage can be seen in

Figure 18, where the two planes shown represent planes of symmetry. The model with applied symmetry is shown in Figure 19, from which a section housing a single window is taken (Figure 20). This section is also symmetric, and can be further reduced to a quarter model by applying a final symmetry as shown in Figure 21.

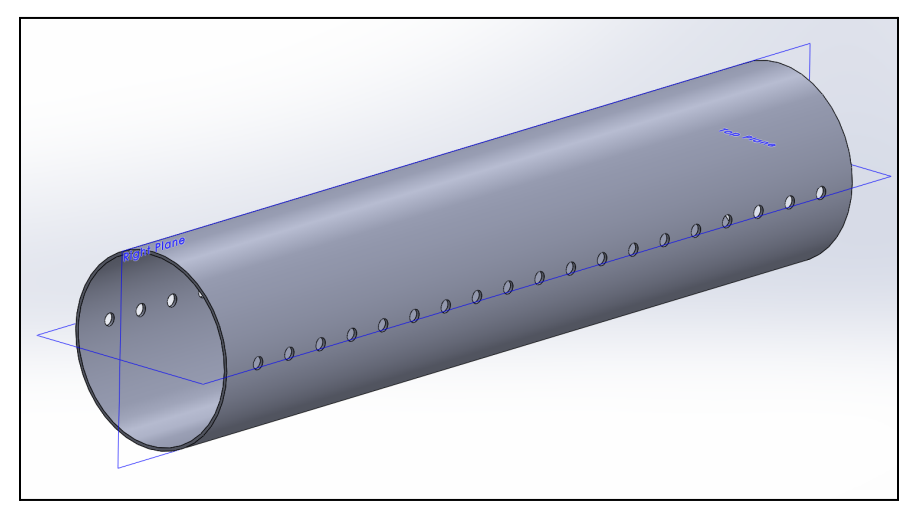


Figure 18: Simplified fuselage model with symmetry planes shown

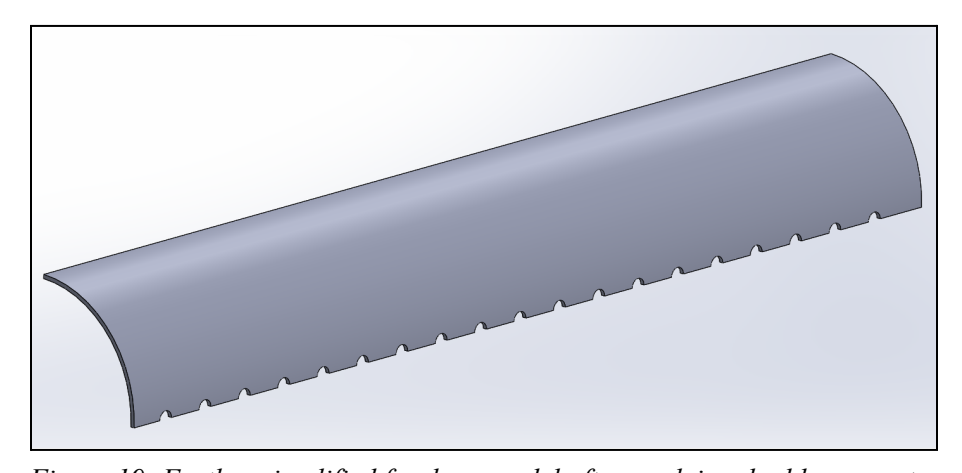


Figure 19: Further simplified fuselage model after applying double symmetry

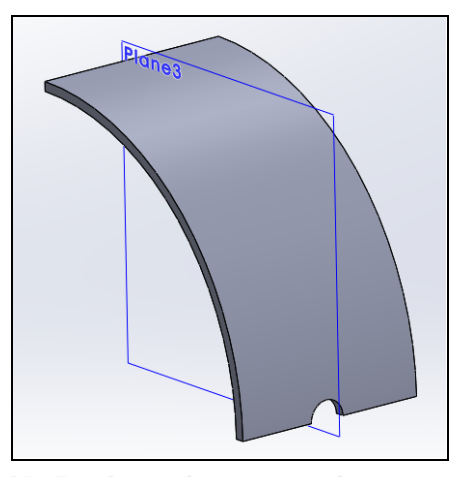


FIgure 20: Single window section showing symmetry



FIgure 21: Final quarter model of window section

# Creating the Mesh

Taking a small section of the fuselage and applying triple symmetry to simplify it results in a model comprising 1/72 of the initial version. This allows for a finer mesh compared to the entire fuselage, which would certainly reach millions of elements if a mesh with the same level of detail applied. The global default for the entire quarter model was set to 100 mm quadratic elements, with body sizing applied via spheres of influence at the centers of the circular (*Figure 22*) and square (*Figure 23*) window holes. The spheres at the center of the square hole were made slightly larger than that of the circular hole to capture the areas of highest stress at the cost of longer simulation times. The mesh statistics can be seen in *Table 3*.

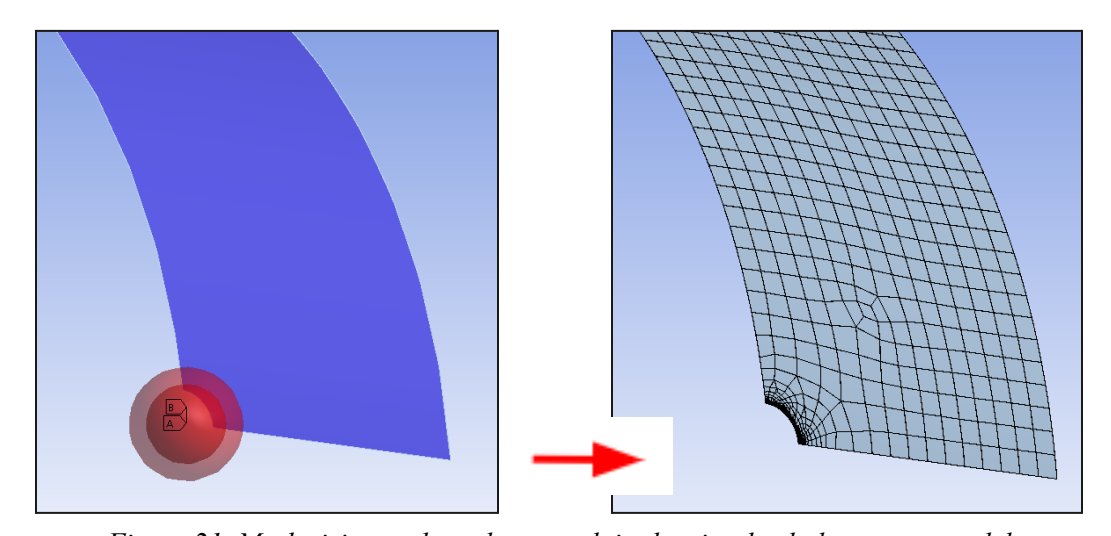
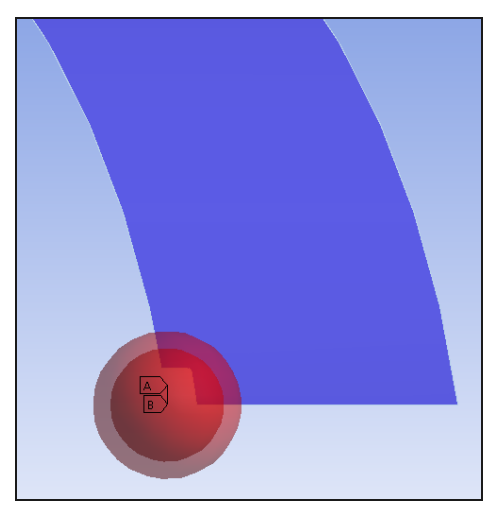


Figure 21. Mesh sizing and resultant mesh in the circular hole quarter model



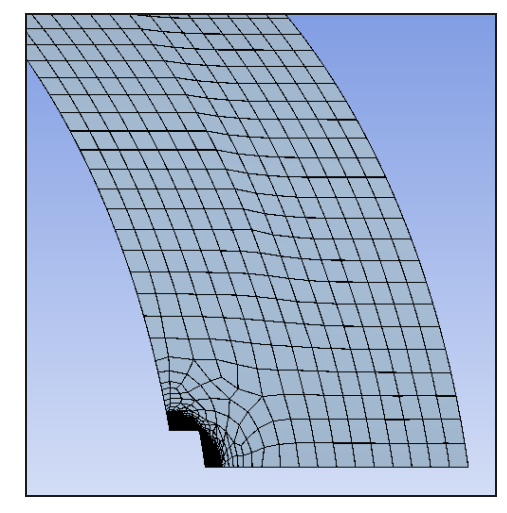


Figure 22. Mesh sizing and resultant mesh in the square hole quarter model

Table 3: Mesh statistics

Hole Type	Sphere Radius 1	Element Size 1	Sphere Radius 2	Element Size 2	# Nodes	# Elements
Circular	175 mm	1 mm	250 mm	20 mm	26479	128690
Square	230 mm	1 mm	300 mm	20 mm	3698	18316

# **Boundary Conditions**

Once the circular and square hole quarter models were finalized and the mesh applied, identical boundary conditions were applied to each. First, three symmetry features were applied at each of the faces where the model was cut. The exact faces where symmetry was applied can be seen as A, B, and C in *Figure 23*, and prevent motion normal to the XZ, YZ, and XY plane respectively. Next, rigid body motion was prevented by applying a cylindrical support on the inner and outer surfaces of the fuselage fixing displacement in the axial and tangential directions while leaving the radial direction free, and is denoted as D in *Figure 23*. The final boundary condition involved applying the gauge pressure of 53,362 Pa on the inner face of the fuselage, shown by E in *Figure 23*.

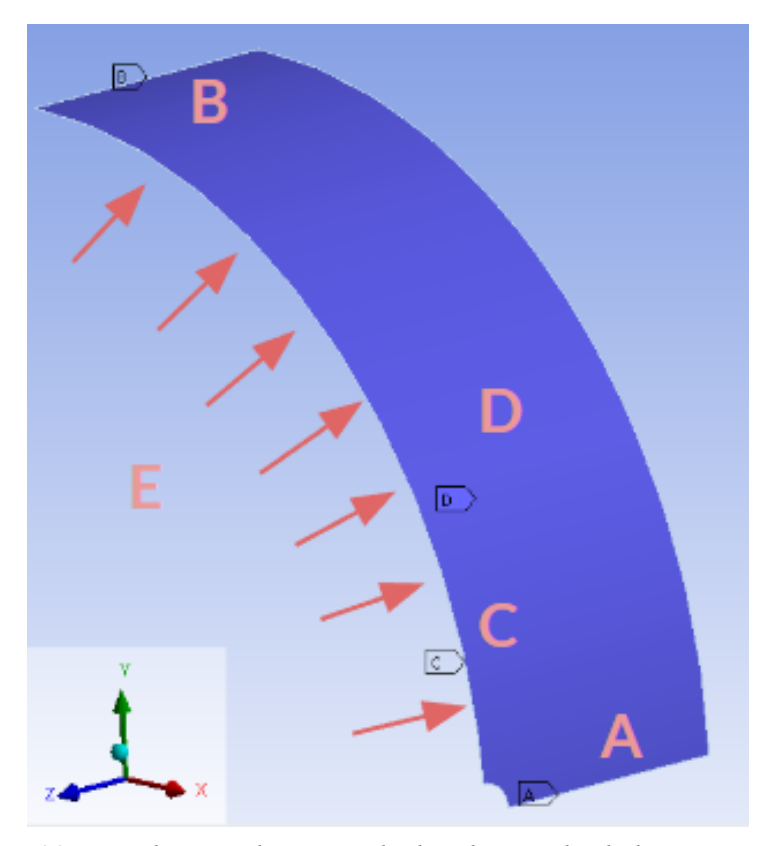


Figure 23. Boundary conditions applied to the circular hole quarter model

#### **Stress Results - Circular Hole**

Running the simulation with the given mesh and boundary conditions yielded the results seen in *Figure 24*, which showed some difference from the analytical results. First, the maximum von Mises stress was approximately 40 MPa greater than the expected value. Similarly, the stress concentration factor  $K_t$  was calculated to be 3.02, higher than the expected ratio of 2.5. As the location of the max stress on the hole was consistent, this difference in magnitude was attributed to the flat plate assumption used in the analytical solution, which will be further discussed in a later section. Next, there was variation in the tangential and shear stresses in both the magnitude and location of the maximum stress. In the shear stress result specifically, the expected location of the maximum stress was 135°, which was not visible on the quarter model. If this study were to be repeated, it would be advisable to obtain results from a half model where symmetry about the XY plane was not taken to observe the distribution of stress around the hole ranging from 0 to 180°. It was found that using the half model compared to the quarter model gave similar maximum stresses, so the inclusion of this symmetry plane is assumed not to be the source of the difference of magnitude.

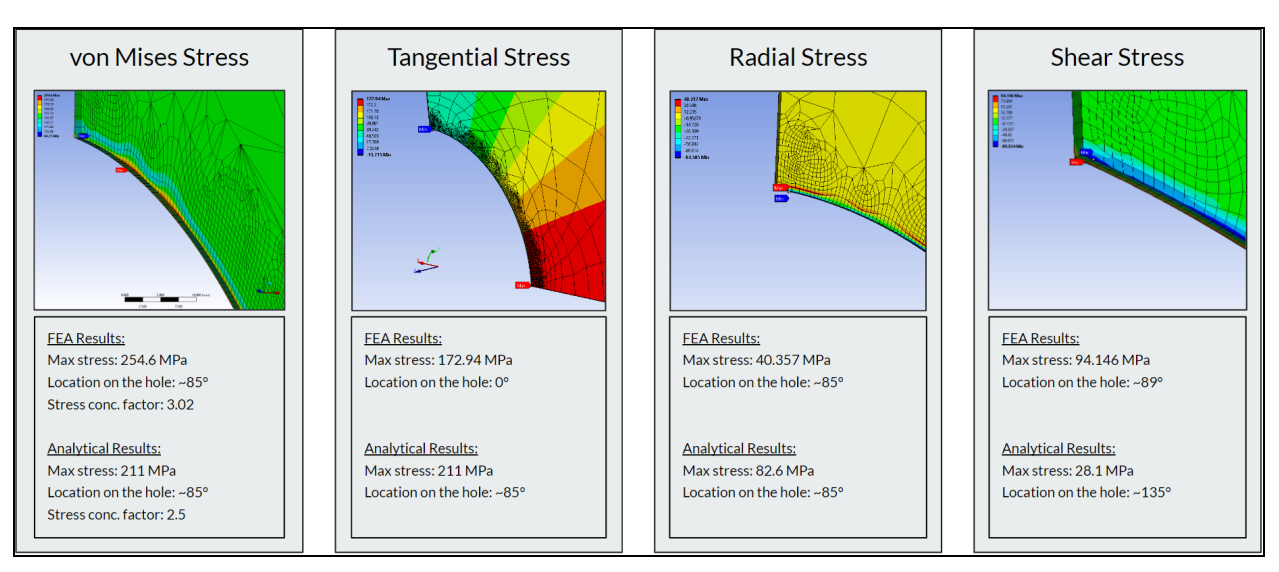


FIgure 24. Comparison of FEA results to expected values from the analytical solution

#### **Stress Results - Square Hole**

For initial simulation results of the stress distributions around the square hole, the maximum fillet radius of 152 mm was used so the results may be comparable to that of the circular hole as shown in Figure 25. While the true maximum fillet radius is 152.5 mm, inputting this value caused errors in Ansys as the line endpoints converged. It was then determined that a half millimeter smaller fillet radius would provide similar enough results. The maximum von Mises stress around the square hole showed only a 2.7% error compared to the same result for the circular hole, and a 23.9% error compared to the expected value from the analytical calculation. The tangential stress showed an 8.8% error compared to that of the circular hole, and a 10.8% error when compared to the analytically derived value. Radial and shear stress results for the square hole showed greater differences when compared to the circular and analytical solutions, with the maximum shear stress once again being located in the first quadrant, matching the case with the circular hole but not comparable to the results given by the analytical approach.

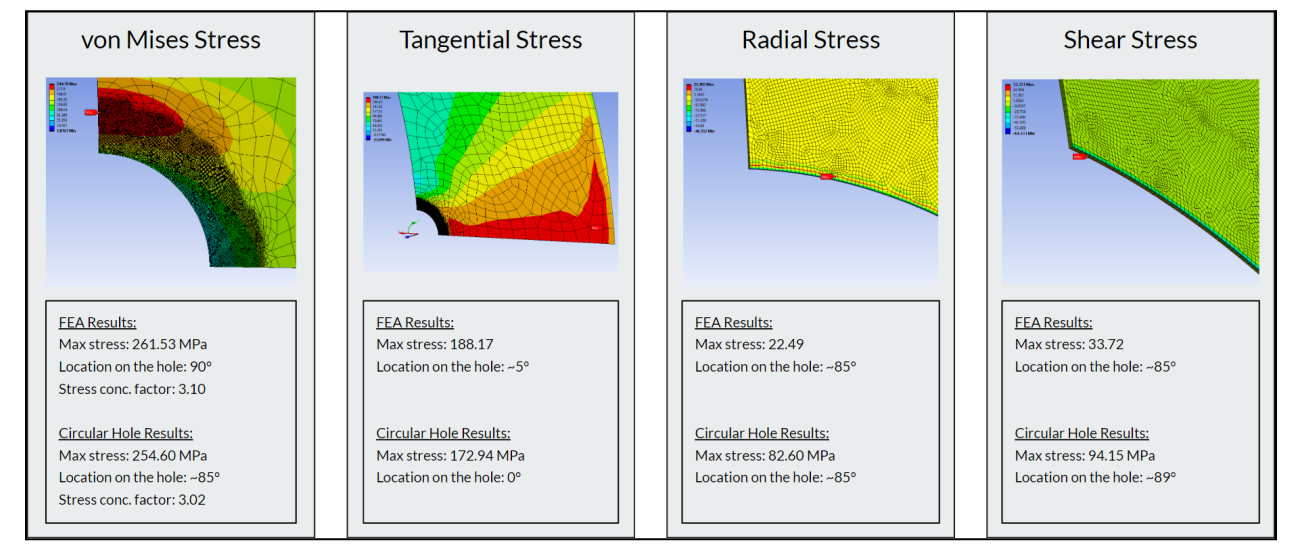


FIgure 25. Comparison of square hole FEA results to expected values from circular hole FEA results

# **Sensitivity Study**

It would stand to reason that a square hole with a fillet radius equal to the radius of the circular hole should give the same stress distribution results. It is also known that a square hole with no fillet would yield stress singularities, or areas of infinite stress. Given these facts, one can intuit that the maximum stress due to stress concentration will decrease as the fillet radius increases. While it is most likely not a linear relationship, it is expected to see the maximum stress reach a minimum value upon the fillet radius reaching its maximum value.

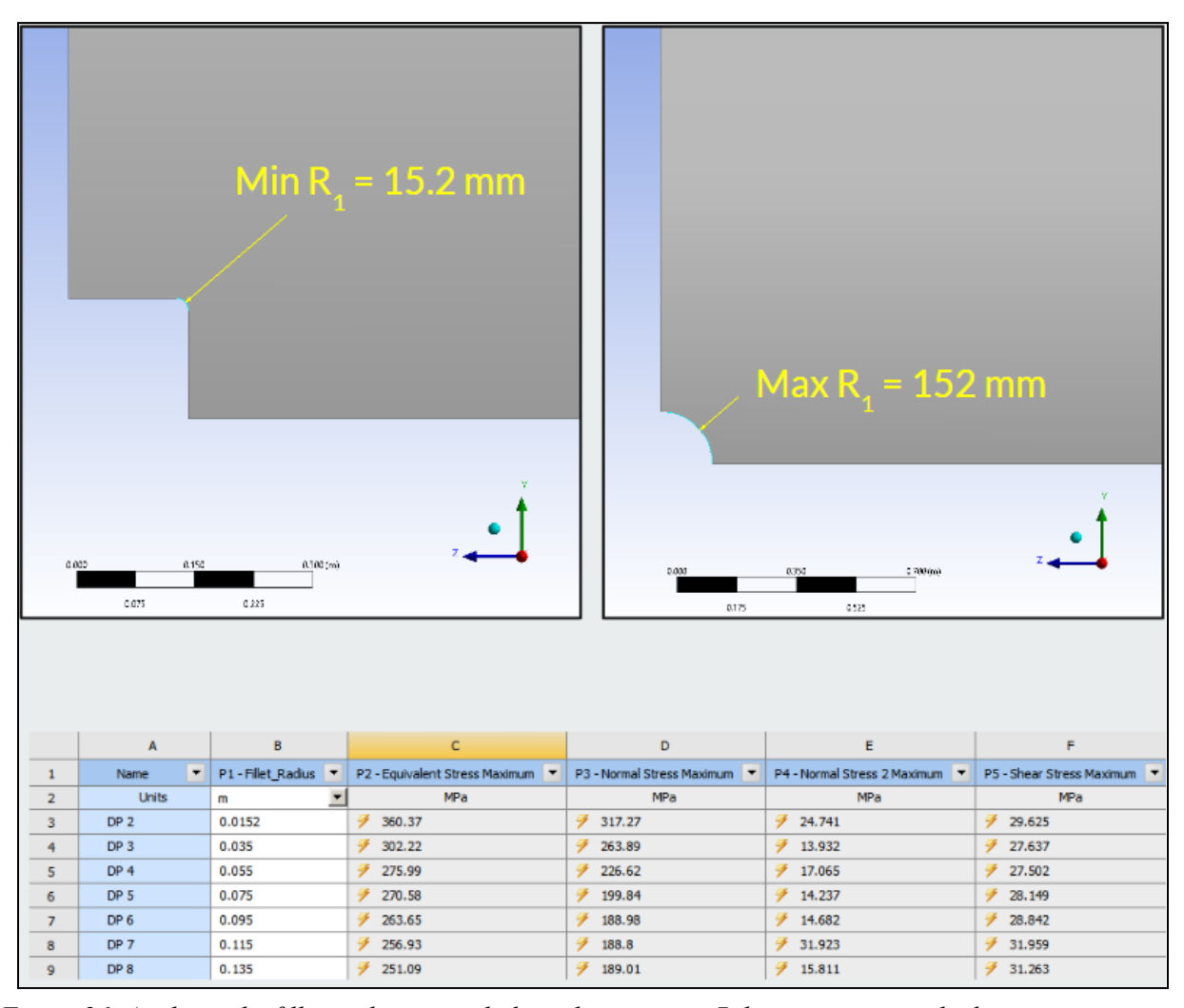


Figure 26. Applying the fillet to the square hole and generating 7 design points at which to compute stress

By selecting the fillet radius as an input parameter along with von Mises stress, tangential stress, radial stress, and shear stress as output parameters, the parameter set was established. Then, 7 custom fillet radius design points in regular intervals of 20 mm were generated. Upon conducting the sensitivity study and varying the fillet radius from 15.2 to 152 mm, an unintuitive behavior was observed. The maximum stress reached a minimum at 0.135 mm, then began increasing again. As  $K_t$  is proportional to maximum stress, the same behavior was observed. However the tangential stress did exhibit the expected behavior

as it asymptotically approached approximately 188 MPa all the way to 152 mm. The difference between von Mises and tangential stresses near the maximum fillet radius was believed to be due to influences from the radial and shear stresses in the calculation of the von Mises stress, as those values show an overall increase as fillet radius increased.

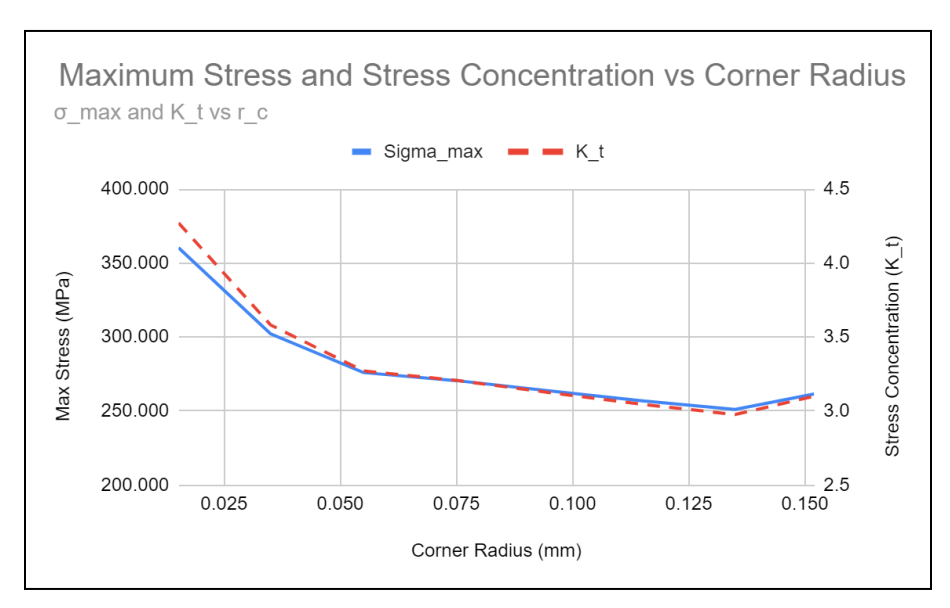


Figure 27. Unintuitive evolution of von Mises stress showing a rise at the maximum fillet radius

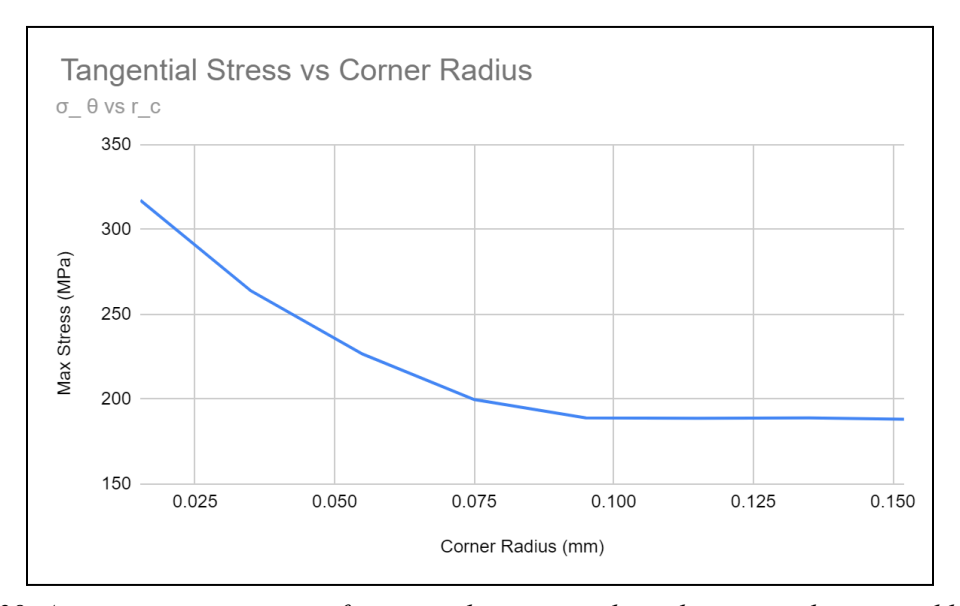


Figure 28. Asymptotic progression of tangential stress matching the intuitively expected behavior

Evaluating the stresses at a fillet radius 30.5 mm gives a maximum stress of 347.63 MPa and a stress concentration factor of 4.12, an 8% difference when compared to the value of 3.79 obtained by Roark's formulation with uniaxial loading in the analytical approach. This is consistent with the other von Mises and tangential stress results being higher in the FEA solution than the analytical solution for both the

circular and square hole. The persistence of this error between both geometries suggests a source of systematic error affecting the FEA solutions, and is explored in the following section.

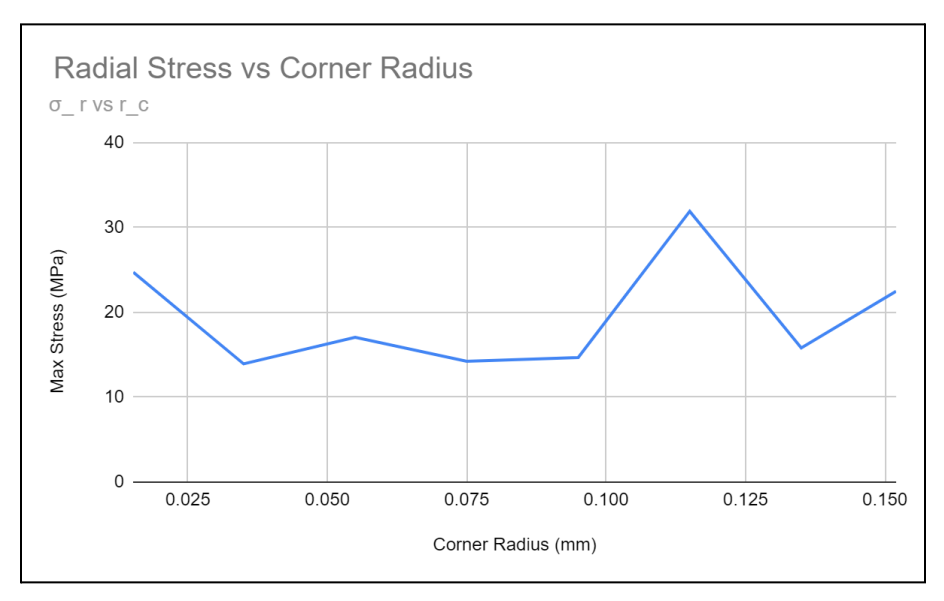


Figure 29. Radial stress sensitivity due to increasing fillet radius

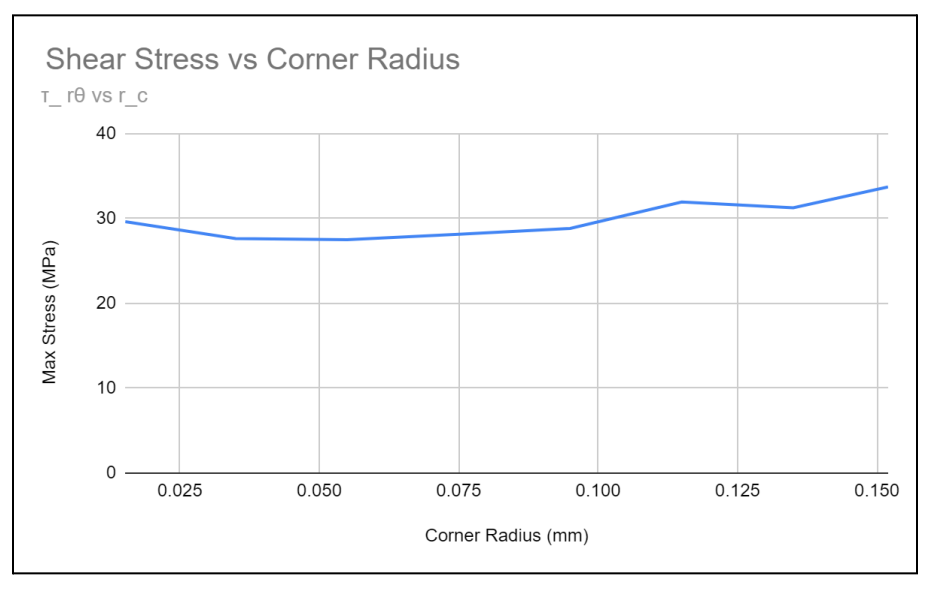


Figure 30. Shear stress sensitivity due to increasing fillet radius

# **Error Analysis**

In the analytical solution, the hoop and longitudinal stress in the fuselage is calculated using the formulae for an close-ended thin-walled cylinder. These stresses are then defined as biaxial loads on a semi-infinite domain. This problem is then solved using the principle of superposition to give the stress concentration factor of 2.5 for the circular window. When attempting to recreate this configuration in Ansys, the obtained results were vastly different from the expected values, and could not be improved. Following

this, the longitudinal stress was removed from the FEA model. This meant that the FEA model was obtaining results for an open-ended cylinder when the analytical solution assumed a close-ended cylinder. This undoubtedly caused error when obtaining the stress distribution and concentration factors and is confirmed by noticing that the stress concentration factor in the circular hole of 3.02 matches the expected value of 3 for a case with uniaxial loading. While this means the results are not directly comparable, they should still be somewhat similar as the longitudinal stress is half of the hoop stress, meaning it has less of an impact on the results than the hoop stress does.

Due to how the stresses were taken from the thin-walled cylinder and applied to the semi-infinite domain, there is also a source of error due to the conversion from a curved domain to a flat one. To understand how much this affects the results, the semi-infinite section was modeled as a flat plate in Ansys with no symmetry taken as shown in Figure 31. The radial gauge pressure was replaced with a vertically applied uniaxial pressure of 84.312 MPa which resulted in a maximum stress of 227.75 MPa and a stress concentration factor of 2.70. Compared to the maximum stress of 245.6 MPa and  $K_t = 3.02$ , it is clear to see that the curve of the plate contributes about 11% error when assuming the semi-infinite domain is flat.

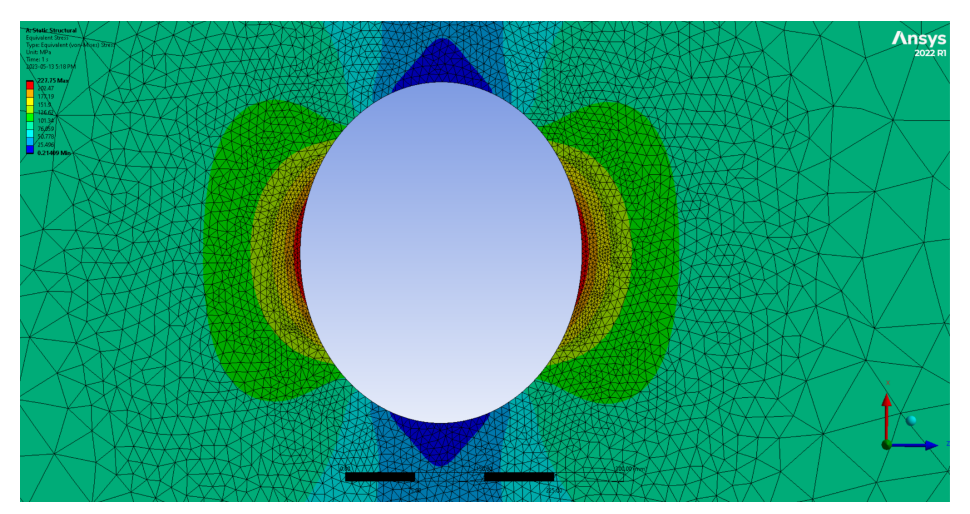


Figure 31. Uniaxial loading flat plate with circular hole (k = 2.70)

The same configuration of loading and boundary conditions was used to simulate a uniaxially loaded flat semi-infinite domain with square hole with a 30.5 mm fillet as shown in *Figure 32*. The simulation returned a max stress of 330.72 MPa and  $K_t$  of 3.92, leading to about 5.1% error in the stress 3.3% error in  $K_t$  when compared with the curved plate solutions of the same case, confirming the hypothesis that the curve in the plate affects the stress distribution results in both the circular and square hole cases.

Given the results presented in the report, three sources of error are evident. First, the removal of the longitudinal stress in Ansys due to the closed ends of the fuselage. Second, the assumption that the stress results will be equal in the flat and curved plate. Finally, there is likely an error in the boundary conditions due to the variance in results and difficulties with applying the longitudinal stress. If this project were to be redone from the beginning, these three areas would be the main focuses to improve the results of and comparison between the analytical and numerical solutions.

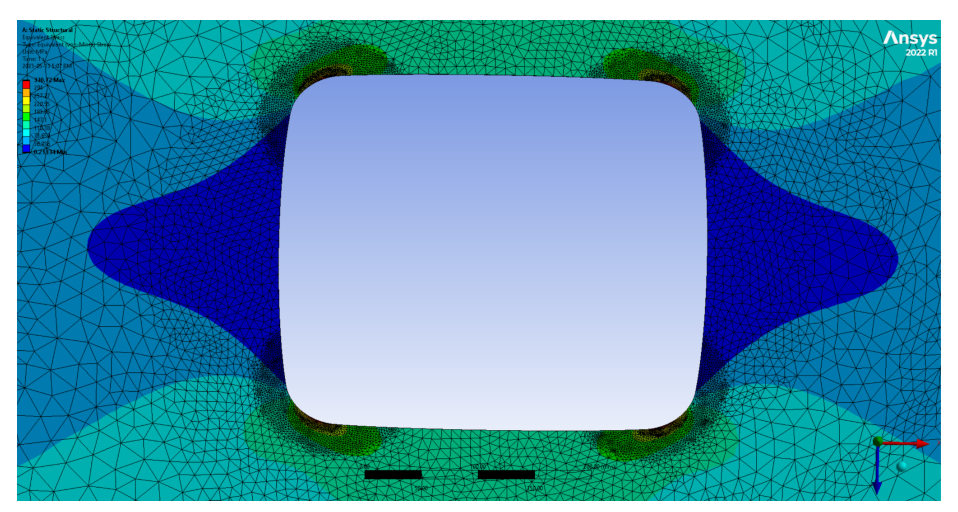


Figure 32. Uniaxial loading flat plate with square hole (k = 3.92)

# **Experimental Validation**

Experimental validation of stress concentrations around airplane windows can be achieved through a variety of physical tests. Since commercial jet airplanes have now been around for over 70 years, the modifications and engineering developments have gone through numerous iterations. With these iterations, it is very rare that an entire structural overhaul of an airplane will take place, but minor iterations to window shape may be made. Since the cost of a single airplane is well into the price range of tens to hundreds of millions of dollars, and safety is of the utmost importance, airliners must prioritize testing and validation (Walsh). The following are some potential non-destructive methods used to experimentally validate the stress concentrations around passenger windows found in the analytical solution and FEA results.

Full-scale testing of an entire aircraft fuselage or a representative section with window cutouts can provide valuable data to validate the FEA model. This can involve subjecting the fuselage to aircraft pressurization equipment ("Aircraft Pressurization Equipment | Order Cabin Pressurization Equipment for ATA-21 Air Conditioning & Cabin Pressure Testing"). Every commercial airplane is pressure tested before taking flight. When engineering these aircrafts, these same tools could be used to simulate flight pressures and identify regions of high stress.

Attaching strain gauges near the window cutouts on a representative test model or a full-scale fuselage section can provide direct measurement of local strains. The results can then be compared with the FEA model to determine the accuracy, identify potential discrepancies, and assess the reliability of both methods.

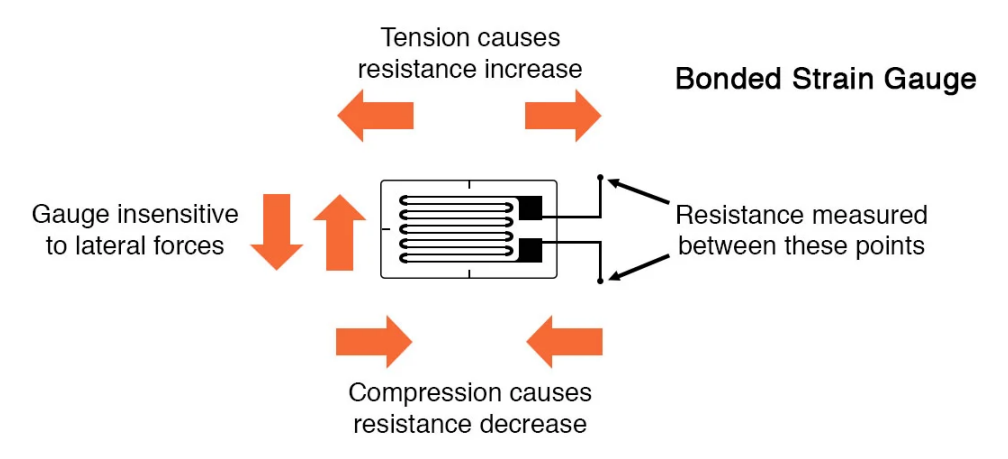


Figure 33: Bonded Strain Gauge Diagram ("Strain Gauges | Electrical Instrumentation Signals | Electronics Textbook")

Another form of experimental validation could be digital image correlation (DIC). This is an optical measurement technique that uses a series of digital images taken over a period of time that tracks the displacement of individual points of a surface. The surface of the representative section of the airplane is first painted white, and black spots are then painted across the entire surface. Two cameras are then set up to capture a 3D model of the test subject, and the output of the experimental displacement can then be related to stress within the airplane skin.

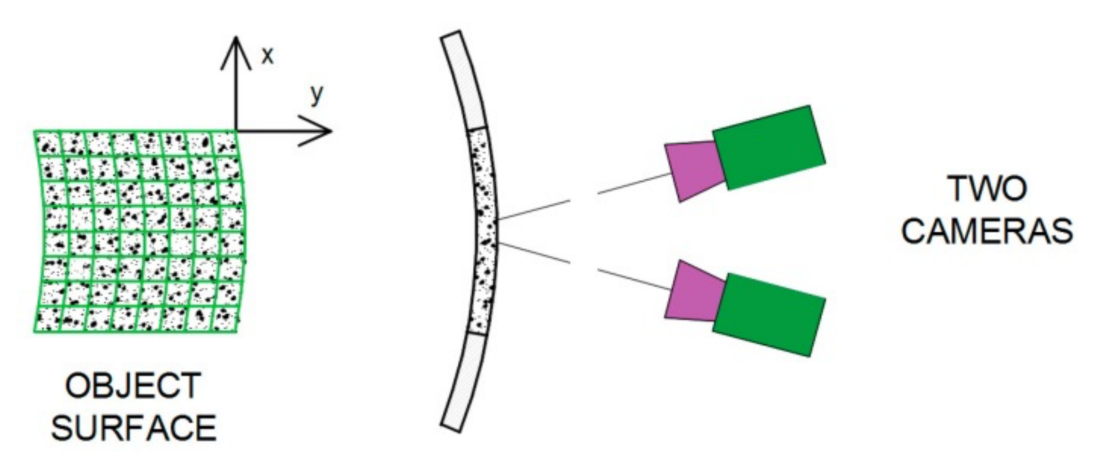


Figure 34: DIC diagram ("Application of Digital Image Correlation (DIC) Method for Road Material Testing")



Figure 35: DIC testing on an aircraft fuselage (Roper)

Comparing these experimental validation methods to the analytical and FEA results, the assumptions made in both the analytical method and FEA method may yield different results. In a full-scale model the fuselage beneath the airplane skin will likely constrain the skin more than what is assumed in the models. The fuselage subframe around the window cutouts likely has a high safety factor, as well as the rest of the aircraft. The influence of fatigue, friction, and external air turbulence that have been assumed to be negligible for the purpose of this report, certainly have a large impact on the stresses on the exterior of aircrafts. Another assumption that was made is that the aircraft skin is assumed to have the gauge pressures applied to it. This is an accurate assumption, as it is the airplane skin that is responsible for sealing the cabin. With this, the airplane skin has much more reinforcing than what is assumed in the FEA model. Finally, looking at the single part, a section of aircraft skin, rather than the entire assembly of an aircraft fuselage, does not account for the complexity of the overall problem.

In total, these experimental validation methods are likely a part of various other testing that is done simultaneously with the same full-scale model. The equipment used for pressure testing aircrafts likely costs hundreds of thousands of dollars, and are capable of accurately simulating high-altitude situations that include significant data collection from the testing. A majority of the costs associated with pressurization testing are accrued from the capital cost of testing equipment that can be used repeatedly (*Table 4*).

Table 4: Experimental validation estimated cost.

Item	Description	<b>Estimated Cost</b>	
DIC Equipment	Digital imaging correlation equipment. This cost includes cameras, setup, paint, and analysis software ("Aerospace Industry Services Contact Page").	\$50,000	
Strain gauges	Includes the cost of several strain gauges and the associated data collection equipment used in the aerospace industry ("Contact us about sales and service").	\$20,000	
Labour	Includes engineering, technician, data analysis	\$100,000	
Full-scale model	This full scale model will likely be used for numerous tests, not specific to testing stress concentration around the passenger windows.	\$100,000	
Testing Facility	This cost is assumed to be a fraction of the cost assumed to be associated with the cost of building a testing facility for the testing of an entire aircraft.	\$100,000	

Note, these costs are not the cost per test, rather the capital cost of the equipment required to perform the test. Due to the nature of this industry, accurate pricing is not readily available and educated approximations are made. For more accurate pricing, links have been provided for pricing requests from respective suppliers.

#### **Conclusions**

In conclusion, it was found that the geometry of a square window that induces the lowest stress for uniaxial loading had a corner radius over width ratio ( $r_c/b$ ) of 0.7. The stresses around a square window with ratio of 0.2 induces stress that are 1.75 times higher than for a circular window ( $r_c/b = 1$ ). This shows the importance of avoiding sudden geometry changes to avoid high stresses. In this project, the circular window is preferred over a square window. The analytical solutions and the FEA solutions for a flat plate under biaxial loading and a square plate under uniaxial loading are consistent in accuracy. However, comparing the analytical solution with the FEA for the curved plate stresses are significantly different. Due to the curvature, stresses are 11% higher in FEA than calculated in the analytical solution. Hence, the flat plate assumption is underestimating the stress. Finite element analysis provides stress results that are based on less assumptions and are therefore more realistic. To solve stress problems similar to this project, it is recommended to use FEA. In addition, experimental validation should be used, such as strain gauges or digital image correlation, to validate the FEA and/or analytical results.

# Acknowledgement

Thanks to ANSYS, Inc for providing the finite element analysis software.

#### **Works Cited**

- "Aircraft Pressurization Equipment | Order Cabin Pressurization Equipment for ATA-21 Air Conditioning & Cabin Pressure Testing." *Tronair*,

  https://www.tronair.com/products/air-conditioning-and-cabin-pressure-testing-ata-21/cabin-pressure. Accessed 9 May 2023.
- 'Ansys Workbench 2021 R2®: Ansys/Ed Student Edition' (1998). ANSYS, Inc.
- "Application of Digital Image Correlation (DIC) Method for Road Material Testing." *NCBI*, 24 July 2019, https://www.ncbi.nlm.nih.gov/pmc/articles/PMC6696109/. Accessed 11 May 2023.
- Beresnevicius, Rytis, and Rosita Mickeviciute. "Aircraft That Brought The Future de Havilland Comet." *AeroTime*, 11 February 2019, https://www.aerotime.aero/articles/23055-aircraft-brought-future-de-havilland-comet. Accessed 9 May 2023.
- "De Havilland DH106 Comet 1 & 2." *BAE Systems*,

  https://www.baesystems.com/en/heritage/de-havilland-comet-1---2. Accessed 9 May 2023.
- "FAA Doesn't Specify How Hot Is Too Hot in a Grounded Airplane." *NBC News*, 15 July 2017, https://www.nbcnews.com/business/travel/faa-doesn-t-specify-how-hot-it-can-be-grounded-n783 346. Accessed 9 May 2023.
- Nageswara Rao, D. K., et al. "Stress around Square and Rectangular Cutouts in Symmetric Laminates." *Composite Structures*, vol. 92, no. 12, Nov. 2010, pp. 2845–59,
  doi:10.1016/j.compstruct.2010.04.010.
- Pan, Zuxing, et al. "Stress Analysis of a Finite Plate with a Rectangular Hole Subjected to Uniaxial

  Tension Using Modified Stress Functions." *International Journal of Mechanical Sciences*, vol.

- 75, Oct. 2013, pp. 265–77, doi:10.1016/j.ijmecsci.2013.06.014.
- Roark, Raymond Jefferson, and Warren Clarence Young. *Roark's Formulas for Stress and Strain*.

  McGraw-Hill Companies, 1989.
- Roper, Jack. "Digital image correlation: How and when to use it in aerospace testing." *Aerospace Testing International*, 25 March 2021,

  https://www.aerospacetestinginternational.com/features/how-digital-image-correlation-is-maturin

g-into-an-accurate-and-trusted-tool-for-aerospace-engineers.html#prettyPhoto. Accessed 11 May 2023.

- "Strain Gauges | Electrical Instrumentation Signals | Electronics Textbook." *All About Circuits*, https://www.allaboutcircuits.com/textbook/direct-current/chpt-9/strain-gauges/. Accessed 11 May 2023.
- Syracuse Hancock International Airport. "Syracuse Hancock International Airport Airplanes have been referred to as time travel devices. If you'd like to travel in the correct time locally, be sure to spring ahead one hour into Daylight Saving Time tonight. "Facebook, 12 March 2022, https://zh-cn.facebook.com/Syracuse.Hancock.International.Airport/photos/a.279251518899668/2143106575847477/. Accessed 8 May 2023.
- Walsh, Sean. "How Much Does a Commercial Plane Cost? (2023 Prices)." *Pilot Passion*, 18 March 2023, https://pilotpassion.com/how-much-does-a-commercial-plane-cost/. Accessed 11 May 2023.
- Williams, James. "The Arthropod's Revenge | How the Airplane's Fuselage Has More in Common with Bugs than Birds." *I Fly America*, 14 May 2023, https://www.google.com/url?q=https://iflyamerica.org/maintenance\_airplane\_fuselage.asp&sa=D

& source = docs & ust = 1684120843767461 & usg = AOvVaw0 HAoVnIi GiMES HALpuvb8R.

# Appendices

**Appendix A: MATLAB Code and Figures** 

■ ME260\_ProjectMATLAB.pdf

MATLAB mlx-file